



## Full Length Article

Atomic-layer-deposited ZrO<sub>2</sub>-doped CeO<sub>2</sub> thin film for facilitating oxygen reduction reaction in solid oxide fuel cellByung Chan Yang<sup>1</sup>, Dohyun Go<sup>1</sup>, Seongkook Oh, Jeong Woo Shin, Hyong June Kim, Jihwan An\*

Department of Manufacturing Systems and Design Engineering (MSDE), Seoul National University of Science and Technology, Republic of Korea

## ARTICLE INFO

## Keywords:

Low-temperature solid oxide fuel cell  
Zirconia-doped ceria  
Atomic layer deposition  
Cathode interlayer

## ABSTRACT

Ultra-thin ZrO<sub>2</sub>-doped CeO<sub>2</sub> (ZDC) interlayers (20 nm thick) with varying doping ratios of 0, 20, and 60 mol% were prepared using atomic layer deposition (ALD), and were investigated as cathodic interlayers for low-temperature solid oxide fuel cells (LT-SOFCs). The inclusion of ZrO<sub>2</sub> in CeO<sub>2</sub> film induced the reduction of Ce<sup>4+</sup> to Ce<sup>3+</sup> with higher concentration of oxygen vacancies, and also enhanced the resistance of the film to the coarsening at elevated temperature (800 °C), well preserving the nanoscale fine grain structure. As a result, the maximum power density of the cell with 20 mol%-doped ZDC interlayer improved by 57% compared to the cell without the interlayer due to enhanced activation process at the cathode, which seems to be due to higher oxygen vacancy population as well as higher grain boundary density at the electrolyte-cathode interface.

## 1. Introduction

Solid oxide fuel cells (SOFCs) are attractive candidates as next-generation energy conversion devices because they are highly efficient and eco-friendly, and can be operated with various fuels ranging from hydrogen to hydrocarbons. Conventional SOFCs, however, are usually operated at temperature above 800 °C and have problems with thermal durability and material selection for thermal shielding [1–3]. Therefore, the research on low-temperature SOFC (LT-SOFC) operated under 500 °C has been active [4,5]. At low temperatures, however, the activation process at the interface between electrolyte and electrode dramatically slows down, particularly at the cathode-electrolyte interface due to high activation energy (~1 eV) of oxygen reduction reaction (ORR) [6]. Adopting the material to expedite the cathodic activation process, therefore, is crucial in improving the LT-SOFC performance.

CeO<sub>2</sub>-based material is known to facilitate the ORR because of its high surface exchange coefficient as well as high oxygen-ion conductivity [7,8]. One can further enhance the oxygen exchange activity of CeO<sub>2</sub> by doping it, which can additionally benefit the stability of the material [9,10]. For example, doping CeO<sub>2</sub> with chemically stable ZrO<sub>2</sub> is known to induce the formation of structural defects, and therefore improves oxygen mobility or oxygen storage capacity (OSC) [11,12]. Due to such properties, ZrO<sub>2</sub>-doped CeO<sub>2</sub> (ZDC) has been studied for applications such as three-way catalytic converters [13–15]. Relatively

recently, researchers have applied the ZDC layer to various novel electrochemical devices such as SOFCs or lithium-air batteries. Liao and Wang have adopted Ni-ZDC mixture as anode catalyst material for ethanol oxidation in SOFCs [16,17]. Moreover, Kalubarme and Ahn have shown that the ZDC can help to facilitate the ORR in lithium-air batteries [18–20].

While ZDC has been mostly prepared by using conventional bulk methods such as sintering in previous researches, atomic layer deposition (ALD) can be an interesting and novel tool to fabricate ZDC in ultra-thin film form for precise and delicate modification of surface where most of catalytic reactions occur. ALD owns unique capabilities to deposit ultra-thin films conformally on complex 3-dimensional structures due to surface-limited reaction mechanism, while easily varying the composition by changing the cycle ratio between different materials [21]. ALD, therefore, is extremely useful in atomically mixing materials in thin films, and enables us to investigate the effect of doping level on the film's property at ultra-thin thickness range (i.e., < a few tens of nm).

In this paper, we report the fabrication of ultra-thin ALD ZDC films (~20 nm) with varying doping levels (0, 20, and 60 mol%-doped), and the characterization of their electrochemical properties by applying them as LT-SOFC's cathodic interlayers. We, for the first time, investigate the applicability of ALD ZDC layer to LT-SOFCs and elucidate the doping effect of ultra-thin ZDC films on their electrochemical

\* Corresponding author at: Department of Manufacturing Systems and Design Engineering, Seoul National University of Science and Technology, 232 Gongneung-ro, Nowon-gu, Seoul 139-743, Republic of Korea.

E-mail address: [jihwanan@seoultech.ac.kr](mailto:jihwanan@seoultech.ac.kr) (J. An).

<sup>1</sup> These authors contributed equally to this work.

performances. We further demonstrate the improvement in thermal stability of ALD ZDC films compared to undoped  $\text{CeO}_2$  films upon thermal annealing, which reveals that the doping helps to preserve catalytically-active surface grain boundaries of the films. Finally, we successfully demonstrate that the optimally-doped (i.e., 20 mol %-doped) ALD ZDC cathodic interlayer can effectively reduce the activation resistance of the SOFC by 70% compared to the cell without the interlayer, and therefore, improve the peak power density by 57%.

## 2. Experimental

### 2.1. ALD ZDC film fabrication

For ALD of ZDC films, tetrakis(ethylmethylamido)zirconium(IV) and tris(isopropylcyclopentadienyl)cerium were used as metal precursors for  $\text{ZrO}_2$  and  $\text{CeO}_2$  processes, respectively. Deionized water was used as oxidant. The evaporation temperature of Zr and Ce precursors were kept at 70 °C and 150 °C, respectively, while water was kept at room temperature. The deposition temperature was set at 200 °C. Nitrogen ( $\text{N}_2$ ) gas of 20 sccm was used for purging. Process sequences of  $\text{ZrO}_2$  and  $\text{CeO}_2$  processes were as follows: 0.3 s Zr precursor pulse-30 s  $\text{N}_2$  purge-0.1 s water pulse-30 s  $\text{N}_2$  purge for  $\text{ZrO}_2$  process, and 0.5 s Ce precursor pulse-30 s  $\text{N}_2$  purge-0.1 s water pulse-30 s  $\text{N}_2$  purge for  $\text{CeO}_2$  process. The growth-rate per cycle (GPC) of ALD  $\text{ZrO}_2$  and  $\text{CeO}_2$  processes at the deposition temperature were  $\sim 1.0 \text{ \AA}/\text{cycle}$  and  $\sim 3 \text{ \AA}/\text{cycle}$ , respectively, which are similar to the values reported in previous literatures [21,22].

### 2.2. SOFC sample preparation

For the fabrication of LT-SOFCs with ZDC interlayers, ALD ZDC films were deposited on one side of 8 mol% yttria stabilized zirconia (YSZ) polycrystalline substrate (300  $\mu\text{m}$ , 1 cm  $\times$  1 cm, MTI Korea). Three types of ZDC interlayers with different  $\text{ZrO}_2$  doping levels were fabricated by varying the ratio of  $\text{ZrO}_2$  and  $\text{CeO}_2$  cycles: the  $\text{ZrO}_2$  vs.  $\text{CeO}_2$  cycle ratio of 0:4 for pure  $\text{CeO}_2$  (namely, Ce1), 1:3 for  $\sim 20$  mol% (21.7 mol%) -doped  $\text{CeO}_2$  (namely, Ce0.8) and 3:1 for  $\sim 60$  mol% (56.3 mol%) -doped  $\text{CeO}_2$  (namely, Ce0.4). 80 nm-thick porous Pt was deposited as electrodes (cathode and anode) on both sides of the electrolyte using DC sputtering in 40 mTorr Ar environment with 300 W DC power. The cross-sectional SEM images of the samples (Ce1, Ce0.8, and Ce0.4) clearly show the structure of porous Pt/ALD ZDC/YSZ substrate with the ALD ZDC film thicknesses of  $23.9 \pm 0.8 \text{ nm}$  (Ce1),  $25.1 \pm 0.6 \text{ nm}$  (Ce0.8), and  $25 \pm 0.6 \text{ nm}$  (Ce0.4) (Fig. S1).

### 2.3. Physical/chemical characterizations of ZDC films

X-ray photoelectron spectroscopy (XPS, ThermoFisher Scientific, K-Alpha+) was used to analyze the stoichiometry of the ZDC films. Crystallinity of the ZDC films was analyzed by using X-ray diffraction (XRD, XRD-D2). For the characterization of thermal stability of the film, Ce1, Ce0.8, and Ce0.4 samples were annealed at 800 °C for 2 h in 1 atm  $\text{O}_2$  atmosphere, and the surface morphology was analyzed before and after annealing by using atomic force microscope (AFM, Veeco, diDimension™ 3100, analyzing window size of 500 nm  $\times$  500 nm).

### 2.4. Electrochemical characterization of SOFCs

Linear sweep voltammetry (LSV) and electrochemical impedance spectroscopy (EIS) technique were conducted to electrochemically characterize the LT-SOFCs at 450 °C using potentiostat (Sp-200, Biologic). Customized chamber was used for the fuel cell test [21]. The anode side of the fuel cell was sealed to the chamber using an Au ring and was supplied with 20 sccm dry hydrogen as fuel, while the cathode was exposed to ambient air. LSV analysis of the fuel cell was measured from open circuit voltage (OCV) to 0.1 V at a scan rate of 20 mV/s. EIS

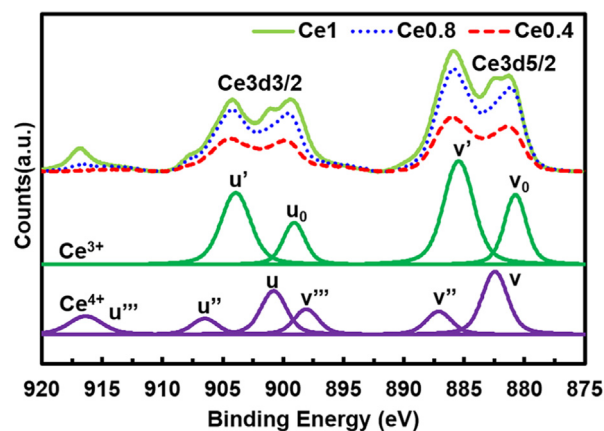


Fig. 1. High-resolution XPS spectra near Ce3d peaks for Ce1, Ce0.8, and Ce0.4 samples. The characteristic spectra for  $\text{Ce}^{3+}$  and  $\text{Ce}^{4+}$  are also shown for comparison [24].

was conducted in a frequency range of 100 kHz to 1 Hz at OCV and a cell voltage of 0.6 V with sinusoidal AC voltage input of 50 mV in amplitude.

## 3. Result and discussion

The compositions of the ZDC interlayers were analyzed by using XPS (Fig. 1). Ce contents of Ce1, Ce0.8, and Ce0.4 samples are 33.9 at%, 27.8 at%, and 14.5 at%, and the Zr contents are 0 at%, 7.7 at%, and 18.7 at%, which confirms the doping levels (i.e., x in  $(\text{ZrO}_2)_x(\text{CeO}_2)_{1-x}$ ) of 0 mol%, 21.7 mol%, and 56.3 mol%, respectively. It is notable that Ce peaks can be divided into characteristic peaks of  $\text{Ce}^{3+}$  and  $\text{Ce}^{4+}$ , and the relative contents of  $\text{Ce}^{3+}$  and  $\text{Ce}^{4+}$  can be calculated (Fig. 1). The spin orbit doublets of ( $v_0$ ,  $u_0$ ) and ( $v'$ ,  $u'$ ) are the characteristic peaks of  $\text{Ce}^{3+}$  and the other peaks are the characteristic peaks of  $\text{Ce}^{4+}$ . Thus, an increase in the intensities of ( $v_0$ ,  $u_0$ ) and ( $v'$ ,  $u'$ ) peaks means that the covariance of  $\text{Ce}^{3+}$  is increased [23]. In Ce1, the mixture of  $\text{Ce}^{3+}$  (62%) and  $\text{Ce}^{4+}$  (38%) is observed even without doping because of the intrinsic formation of oxygen vacancy, i.e.,  $\text{Ce}^{4+}$  reduces to  $\text{Ce}^{3+}$  [24,25]. In ZDC films (i.e., Ce0.8 and Ce0.4), the characteristic peaks of  $\text{Ce}^{3+}$  are even more dominant than those of  $\text{Ce}^{4+}$ , which could be due to structural defects caused by the insertion of Zr into the cubic structured  $\text{CeO}_2$ .  $\text{Ce}^{4+}$  is known to easily reduce to  $\text{Ce}^{3+}$  when the population of structural defects inside  $\text{CeO}_2$  increases by adding  $\text{ZrO}_2$  that has much smaller cations (i.e., ionic radii of  $\text{Zr}^{4+}$ : 8.0 pm,  $\text{Ce}^{4+}$ : 9.7 pm) [11,12].

XRD analysis further elucidates the structural change of the ZDC films when different levels of dopants are included (Fig. 2). Crystalline peaks for cubic  $\text{CeO}_2$  or  $\text{CeO}_2$ - $\text{ZrO}_2$  mixture are clearly observed in all three samples. Interestingly, crystalline peaks have shifted to higher angle as more  $\text{ZrO}_2$  is included; for example, the characteristic peak corresponding to (1 1 1) is 28.5° in Ce1, 29.0° in Ce0.8, and 29.4° in Ce0.4 samples (Inset image of Fig. 2). It is well known that the peak shift in XRD spectra to higher angle implies the decrease of the lattice parameter. By Bragg's law, the relationship between X-ray wavelength ( $\lambda$ , 0.1542 nm), interatomic spacing ( $d_{hkl}$ ) and angle of diffraction ( $\theta$ ) can be expressed as

$$n\lambda = 2d_{hkl}\sin\theta$$

From the XRD results, the interplanar spacings between (1 1 1) crystallographic planes ( $d_{111}$ ) are calculated to be 0.313 nm, 0.307 nm, and 0.303 nm, which leads to the lattice parameters (a) of 0.543 nm, 0.533 nm, and 0.526 nm in Ce1, Ce0.8, and Ce0.4 samples, respectively. This means that the lattice parameter decreases by about 3% in Ce0.4 sample compared to Ce1 sample. We speculate that the structural disorder by the defect formation by  $\text{ZrO}_2$  doping in the  $\text{CeO}_2$  lattice has

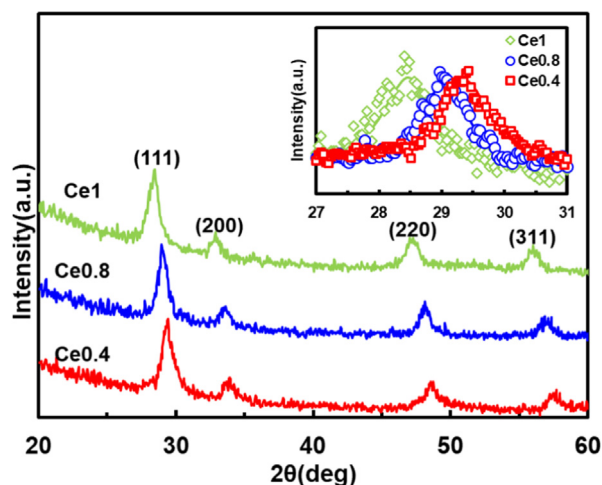


Fig. 2. XRD spectra of Ce1, Ce0.8, and Ce0.4 samples. Inset image shows the high-resolution XRD spectra of the three samples near (1 1 1) peak ( $27^{\circ}$ – $31^{\circ}$ ).

contributed to the shrinkage of the lattice parameter, which matches well to our XPS analysis [9,11,26].

AFM analysis additionally provides interesting observations on microstructural stability (or grain growth) of the ALD ZDC films upon thermal annealing (Fig. 3, Fig S2). Average grain sizes of as-deposited Ce1, Ce0.8, and Ce0.4 films are 30.0 nm, 29.0 nm, and 27.4 nm, respectively. After annealing at  $800^{\circ}\text{C}$  for 2 h in  $\text{O}_2$ -atmosphere, their average grain sizes increase to 39.1 nm, 32.8 nm, and 32.1 nm, respectively. That is, slightly smaller grains are formed in as-deposited ALD ZDC films as the doping level becomes higher; the grain growth also occurs less significantly, i.e., the film becomes more resistant to coarsening upon annealing as the doping level increases. Resultantly, the density of surface grain boundary is well preserved in ZDC films compared to undoped  $\text{CeO}_2$  film both in as-deposited and in annealed samples, which could be beneficial in expediting the oxygen exchange at the surface as will be discussed later in this manuscript. This result also corresponds well to the previous report by Zhang et al., which shows that 20–70 mol% doped ZDC fine nanoparticles in bulk (5–20 nm in size) has the best thermal stability against coarsening at  $800^{\circ}\text{C}$ , while the intrinsic role of  $\text{ZrO}_2$  is not yet fully elucidated [27].

Fig. 4(a) shows current-voltage-power (I-V-P) measurement results of the cells with ALD ZDC interlayers (Ce1, Ce0.8, and Ce0.4) and the cell without interlayer (reference). OCVs of all the cells were similar as 0.99–1.01 V. Maximum power densities were measured as  $3.0\text{ mW}/\text{cm}^2$

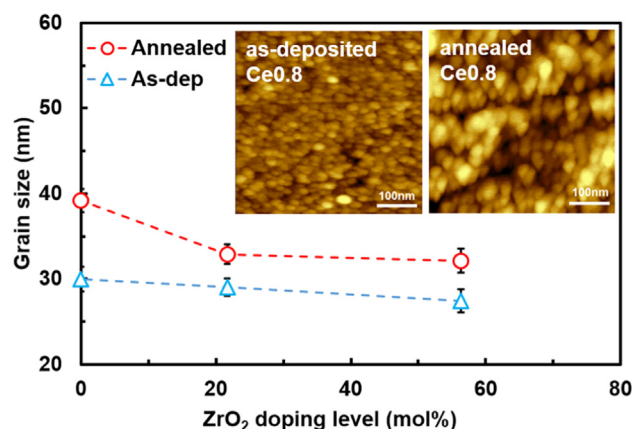


Fig. 3. Average grain size determined from AFM images of as-deposited and annealed samples depending on  $\text{ZrO}_2$  doping level. Inset AFM images represent the surface topography of as-deposited and annealed ( $800^{\circ}\text{C}$ , 2 h) Ce0.8 sample.

for the reference cell without ALD ZDC interlayer, and  $4.0\text{ mW}/\text{cm}^2$ ,  $4.7\text{ mW}/\text{cm}^2$ , and  $4.0\text{ mW}/\text{cm}^2$  for the cells with Ce1, Ce0.8, and Ce0.4 interlayers, respectively. The maximum power density of the cells with ALD ZDC interlayers improved by > 30% compared to that of the reference cell, and especially that of the cell with Ce0.8 interlayer was the highest, i.e., improved by 57% compared to the reference cell.

EIS analysis reveals the individual contributions of the processes in the fuel cell operation (Fig. 4(b-f)). All Nyquist plots in Fig. 4(c-f) are separated into two semicircles: the one that shows the same size regardless of the cell voltage at high frequency range ( $> \sim 10\text{ kHz}$ ), and the other that changes in size depending on the cell voltage at low frequency range ( $< \sim 10\text{ kHz}$ ). The former one can be regarded as ohmic resistance mostly associated with the ohmic transport inside the electrolyte, while the latter one can be regarded as activation resistance, mostly at the cathode due to sluggish cathode reaction compared to anode especially at low temperature regime [28]. The ohmic resistances are similar to each other as  $40 \pm 1.5\ \Omega\text{-cm}^2$ . However, the activation resistance shows the highest value of  $\sim 43\ \Omega\text{-cm}^2$  in the reference cell and the lowest value of  $\sim 13\ \Omega\text{-cm}^2$  in the cell with Ce0.8 interlayer that is 23% lower than that of the cell with Ce1 (i.e., undoped  $\text{CeO}_2$ ) interlayer ( $17\ \Omega\text{-cm}^2$ ) (Fig. 4(b)). EIS analysis clearly confirms our argument that the improved performances of the cell with ALD ZDC interlayers are mainly due to the enhanced activation process at the cathode.

The significant reduction of activation resistance in the ALD ZDC-interlayered cells compared to the reference cell is due to high surface activity of  $\text{CeO}_2$ -based materials as well as high surface grain-boundary density of ALD thin films, which is also observed in previous literatures [7,23]. The enhanced electrochemical performance of the cell with 20 mol%-doped ALD ZDC interlayer (Ce0.8) compared to that with pure  $\text{CeO}_2$  interlayer (Ce1) seems to be ascribed to two aspects: improved surface exchange (or, surface kinetics) by structural defects and better thermal stability against coarsening. The improvement in surface exchange can be explained by the formation of structural defects due to doping, which has been reported to enhance the oxygen diffusion rate and thus the overall kinetic process of ZDC films. Indeed, Zamar et al. reported that the oxygen diffusion and therefore kinetic process on ZDC surface can be promoted by doping  $\text{CeO}_2$  with 20–50 mol%  $\text{ZrO}_2$ , while excessive  $\text{ZrO}_2$  inclusion of > 50 mol% induces almost no effect [9]. Kaspar et al. similarly reported that the excessive inclusion of  $\text{ZrO}_2$  ( $> 50\text{ mol}\%$ ) may cause the tetragonalization to release the lattice stress induced by  $\text{ZrO}_2$  insertion, resulting in a lower oxygen mobility [11]. The thermal stabilization of  $\text{CeO}_2$  by  $\text{ZrO}_2$  insertion has been also observed by other researchers. Pijolat has shown that the doping of  $\text{CeO}_2$  with materials having smaller cation size than that of  $\text{Ce}^{4+}$  can stabilize the  $\text{CeO}_2$  against coarsening [29]. Such enhanced resistance to coarsening can help to maintain the surface grain boundary density at the electrolyte surface in the operation of SOFCs. Surface grain-boundary is known to be more catalytically active compared to the grain-center mainly due to the large population of oxygen vacancies that helps the oxygen exchange or oxygen incorporation at the surface [30]. In conclusion, the combined effect of improved kinetics and thermal stability by  $\text{ZrO}_2$  doping in  $\text{CeO}_2$  seems to have contributed to decrease the polarization resistance at the cathode side of SOFC, which eventually led to the overall electrochemical performance enhancement.

#### 4. Conclusion

We fabricated ALD ZDC thin films with different doping ratios, and investigated the effect of doping on chemical structure as well as thermal stability of the films. Furthermore, we applied the ALD ZDC films to cathodic interlayers for LT-SOFCs, and demonstrated that the activation process at the cathode associated with ORR enhances with the ALD ZDC interlayer. The LT-SOFC with optimally doped (20 mol %)-doped ALD ZDC interlayer showed 70% less activation resistance,

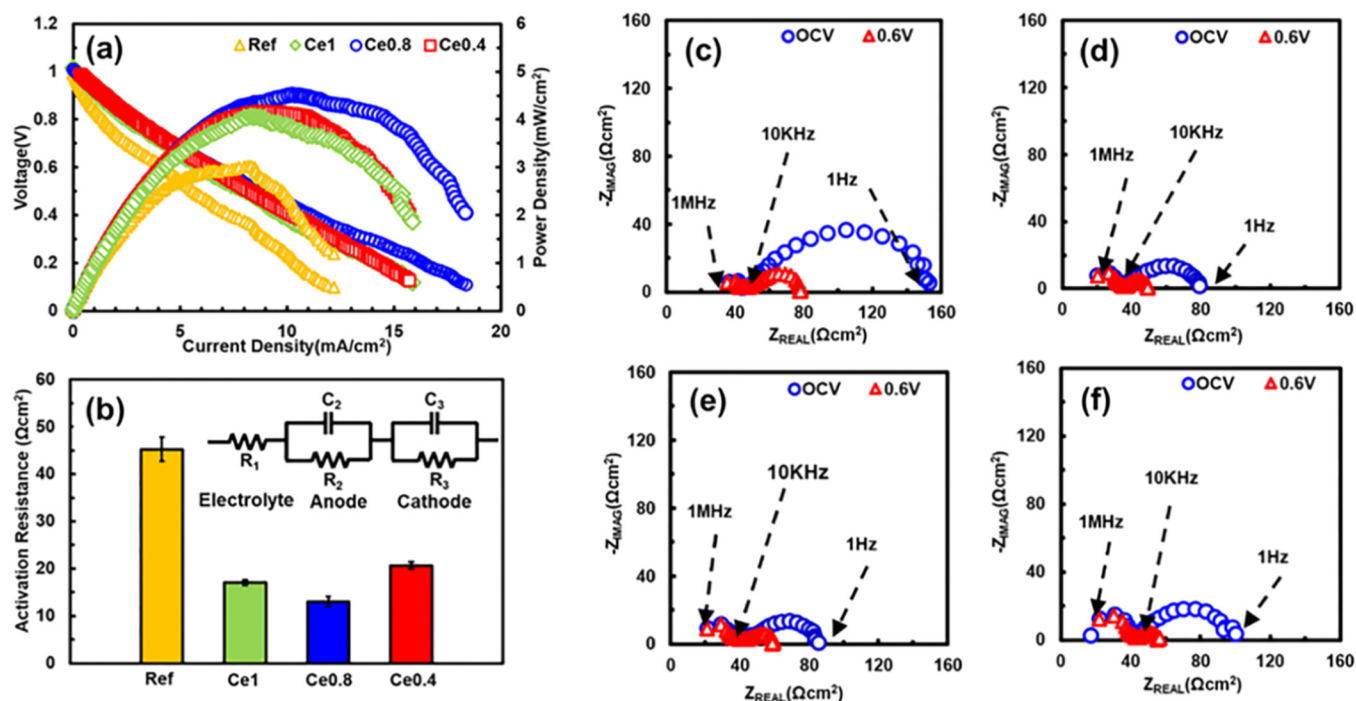


Fig. 4. (a) Polarization curves of the cells without and with ALD ZDC cathodic interlayers at 450 °C. (b) Equivalent circuit model and summarized activation resistances (anode ( $R_2$ ) + cathode ( $R_3$ )) of the cells without (reference) and with ALD ZDC interlayers (Ce1, Ce0.8, and Ce0.4) based on EIS. (c–f) EIS spectra of the cells (c) without (reference) interlayer, and with (d) Ce1, (e) Ce0.8, and (f) Ce0.4 interlayers.

leading to 57% improvement in maximum power density at 450 °C. We attribute such an improvement in activation process at ALD ZDC surface to structural defect formation as well as high surface grain boundary density, both of which seems to be due to  $ZrO_2$  doping. ALD ZDC thin films studied in this paper may find various applications not only in SOFCs but also in other electrochemical devices such as catalytic converters, metal-air batteries, and scrubbers, etc. for better performance and stability even at elevated temperature.

## 5. Notes

The authors declare no competing financial interest.

## Acknowledgements

We acknowledge the financial support from Nano-Convergence Foundation funded by the Ministry of Trade, Industry and Energy (MOTIE) of Korea (No. 20000272) and National Research Foundation of Korea (NRF) grants funded by the Korea government (MSIP) (No. NRF-2018R1C1B6001150). We also thank Dr. Wontae Noh and Air Liquide Laboratory Korea for providing Ce precursors.

## Appendix A. Supplementary material

Supplementary data to this article can be found online at <https://doi.org/10.1016/j.apsusc.2018.12.142>.

## References

- B.C.H. Steele, A. Heinzel, Materials for fuel-cell technologies, *Nature* 414 (2001) 345–352, <https://doi.org/10.1038/35104620>.
- T.M. Gür, Comprehensive review of methane conversion in solid oxide fuel cells: Prospects for efficient electricity generation from natural gas, *Prog. Energy Combust. Sci.* 54 (2016) 1–64, <https://doi.org/10.1016/j.pecs.2015.10.004>.
- E.D. Wachsman, K.T. Lee, Lowering the temperature of solid oxide fuel cells, *Science* 19 (2000) 702740, <https://doi.org/10.1126/science.1204090>.
- E. Wachsman, T. Ishihara, J. Kilner, Low-temperature solid-oxide fuel cells, *MRS Bull.* 39 (2014) 773–779, <https://doi.org/10.1557/mrs.2014.192>.
- Y. Zhang, R. Knibbe, J. Sunarso, Y. Zhong, W. Zhou, Z. Shao, Z. Zhu, Recent progress on advanced materials for solid-oxide fuel cells operating below 500°C, *Adv. Mater.* 29 (2017), <https://doi.org/10.1002/adma.201700132>.
- B.C.H. Steele, Interfacial reactions associated with ceramic ion transport membranes, *Solid State Ionics* 75 (1995) 157–165, [https://doi.org/10.1016/0167-2738\(94\)00182-R](https://doi.org/10.1016/0167-2738(94)00182-R).
- Z. Fan, F.B. Prinz, Enhancing oxide ion incorporation kinetics by nanoscale yttria-doped ceria interlayers, *Nano Letters* 11 (2011) 2202–2205, <https://doi.org/10.1021/nl104417n>.
- H. Inaba, Ceria-based solid electrolytes, *Solid State Ionics* 83 (1996) 1–16, [https://doi.org/10.1016/0167-2738\(95\)00229-4](https://doi.org/10.1016/0167-2738(95)00229-4).
- F. Zamar, A. Trovarelli, C. DeLeitenburg, G. Dolcetti, The direct room-temperature synthesis of  $CeO_2$ -based solid solutions: A novel route to catalysts with a high oxygen storage/transport capacity, 11th Int Congr. Catal. - 40th Anniv. Pts A B 101 (1996) 1283–1292, [https://doi.org/10.1016/S0167-2991\(96\)80340-5](https://doi.org/10.1016/S0167-2991(96)80340-5).
- Y.-I. Lee, Y.-H. Choa, Synthesis and characterization of a ceria based composite electrolyte for solid oxide fuel cells by an ultrasonic spray pyrolysis process, *J. Korean Powder Metall. Inst.* 21 (2014) 222–228, <https://doi.org/10.4150/KPMI.2014.21.3.222>.
- J. Kašpar, P. Fornasiero, M. Graziani, Use of  $CeO_2$ -based oxides in the three-way catalysis, *Catal. Today* 50 (1999) 285, [https://doi.org/10.1016/S0920-5861\(98\)00510-0](https://doi.org/10.1016/S0920-5861(98)00510-0).
- A. Trovarelli, Catalytic properties of ceria and  $CeO_2$ -containing materials, *Catal. Rev. - Sci. Eng.* 38 (1996) 439–520, <https://doi.org/10.1080/01614949608006464>.
- R. Bacani, L.M. Toscani, T.S. Martins, M.C.A. Fantini, D.G. Lamas, S.A. Larrondo, Synthesis and characterization of mesoporous  $NiO_2/ZrO_2-CeO_2$  catalysts for total methane conversion, *Ceram. Int.* 43 (2017) 7851–7860, <https://doi.org/10.1016/j.ceramint.2017.03.101>.
- A.M. Azad, M.J. Duran, Development of ceria-supported sulfur tolerant nanocatalysts: Rh-based formulations, *Appl. Catal. A Gen.* 330 (2007) 77–88, <https://doi.org/10.1016/j.apcata.2007.06.036>.
- A.M. Azad, M.J. Duran, A.K. McCoy, M.A. Abraham, Development of ceria-supported sulfur tolerant nanocatalysts: Pd-based formulations, *Appl. Catal. A Gen.* 332 (2007) 225–236, <https://doi.org/10.1016/j.apcata.2007.08.029>.
- M. Liao, W. Wang, R. Ran, Z. Shao, Development of a Ni-Ce<sub>0.8</sub>Zr<sub>0.2</sub>O<sub>2</sub> catalyst for solid oxide fuel cells operating on ethanol through internal reforming, *J. Power Sources* 196 (2011) 6177–6185, <https://doi.org/10.1016/j.jpowsour.2011.03.018>.
- W. Wang, C. Su, T. Zheng, M. Liao, Z. Shao, Nickel zirconia cerate cermet for catalytic partial oxidation of ethanol in a solid oxide fuel cell system, *Int. J. Hydrogen Energy* 37 (2012) 8603–8612, <https://doi.org/10.1016/j.ijhydene.2012.02.138>.
- R.S. Kalubarme, H.S. Jadhav, C.N. Park, K.N. Jung, K.H. Shin, C.J. Park, Nanostructured doped ceria for catalytic oxygen reduction and  $Li_2O_2$  oxidation in non-aqueous electrolytes, *J. Mater. Chem. A* 2 (2014) 13024–13032, <https://doi.org/10.1039/c4ta01938e>.
- C.H. Ahn, R.S. Kalubarme, Y.H. Kim, K.N. Jung, K.H. Shin, C.J. Park, Graphene/doped ceria nano-blend for catalytic oxygen reduction in non-aqueous lithium-

- oxygen batteries, *Electrochim. Acta* 117 (2014) 18–25, <https://doi.org/10.1016/j.electacta.2013.11.092>.
- [20] R.S. Kalubarme, M.-S. Cho, J.-K. Kim, C.-J. Park, Ceria based catalyst for cathode in non-aqueous electrolyte based Li/O<sub>2</sub> batteries, *Nanotechnology* 23 (2012) 435703, <https://doi.org/10.1088/0957-4484/23/43/435703>.
- [21] S. Oh, J. Park, J.W. Shin, B.C. Yang, J. Zhang, D.Y. Jang, J. An, High performance low-temperature solid oxide fuel cells with atomic layer deposited-yttria stabilized zirconia embedded thin film electrolyte, *J. Mater. Chem. A* 6 (2018) 7401–7408, <https://doi.org/10.1039/C7TA10678E>.
- [22] M. Kouda, K. Ozawa, K. Kakushima, P. Ahmet, H. Iwai, Y. Urabe, T. Yasuda, Preparation and electrical characterization of CeO<sub>2</sub> films for gate dielectrics application: comparative study of chemical vapor deposition and atomic layer deposition processes, *Jpn. J. Appl. Phys.* 50 10PA06 (2011), <https://doi.org/10.1143/JJAP.50.10PA06>.
- [23] J. Bae, Y. Lim, J.-S. Park, D. Lee, S. Hong, J. An, Y.-B. Kim, Thermally-induced dopant segregation effects on the space charge layer and ionic conductivity of nanocrystalline gadolinia-doped Ceria, *J. Electrochem. Soc.* 163 (2016) F919–F926, <https://doi.org/10.1149/2.1201608jes>.
- [24] A. Pfau, K.-D. Schierbaum, The electronic structure of stoichiometric and reduced CeO<sub>2</sub> surfaces: an XPS, UPS and HREELS study, *Surf. Sci.* 6028 (1994) 71–80, [https://doi.org/10.1016/0039-6028\(94\)90027-2](https://doi.org/10.1016/0039-6028(94)90027-2).
- [25] S.R. Bishop, D. Marrocchelli, C. Chatzichristodoulou, N.H. Perry, M.B. Mogensen, H.L. Tuller, E.D. Wachsman, Chemical expansion: Implications for electrochemical energy storage and conversion devices, *Annu. Rev. Mater. Res.* 44 (2014) 205–239, <https://doi.org/10.1146/annurev-matsci-070813-113329>.
- [26] S. Rossignol, D. Duprez, S. Rossignol, Effect of the preparation method on the properties of zirconia – ceria materials, *J. Mater. Chem.* 9 (1999) 1615–1620, <https://doi.org/10.1039/A900536F>.
- [27] F. Zhang, C.-H. Chen, J.C. Hanson, R.D. Robinson, I.P. Herman, S.-W. Chan, Phases in ceria-zirconia binary oxide (1-x)CeO<sub>2-x</sub>ZrO<sub>2</sub> nanoparticles: The effect of particle size, *J. Am. Ceram. Soc.* 89 (2006) 1028–1036, <https://doi.org/10.1111/j.1551-2916.2005.00788.x>.
- [28] J. An, Y.B. Kim, J. Park, T.M. Gür, F.B. Prinz, Three-dimensional nanostructured bilayer solid oxide fuel cell with 1.3 W/cm<sup>2</sup> at 450°C, *Nano Letters* 13 (2013) 4551–4555, <https://doi.org/10.1021/nl402661p>.
- [29] M. Pijolat, M. Prin, M. Soustelle, O. Touret, P. Nortier, Thermal-stability of doped ceria - experiment and modeling, *J. Chem. Soc. Trans.* 91 (1995) 3941–3948, <https://doi.org/10.1039/FT9959103941>.
- [30] J. An, J.S. Park, A.L. Koh, H.B. Lee, H.J. Jung, J. Schoonman, R. Sinclair, T.M. Gür, F.B. Prinz, Atomic scale verification of oxide-ion vacancy distribution near a single grain boundary in YSZ, *Sci. Rep.* 3 (2013) 2680, <https://doi.org/10.1038/srep02680>.